EDGE ARTICLE

Check for updates

Defective blue titanium oxide induces high valence of NiFe-(oxy)hydroxides over heterogeneous interfaces towards high OER catalytic activity†

Tingxi Zhou,‡[a] Yifei Yang,‡[a] Yike Jing,[a] Yuling Hu,[a] Fei Yang,[a] Wei Sun ⓘ *[a] and LeiLei He*[b]

Nickel–iron (oxy)hydroxides ($NiFeO_xH_y$) have been validated to speed up sluggish kinetics of the oxygen evolution reaction (OER) but still lack satisfactory substrates to support them. Here, non-stoichiometric blue titanium oxide ($B-TiO_x$) was directly derived from Ti metal by alkaline anodization and used as a substrate for electrodeposition of amorphous $NiFeO_xH_y$ ($NiFe/B-TiO_x$). The performed X-ray absorption spectroscopy (XAS) and density functional theory (DFT) calculations evidenced that there is a charge transfer between $B-TiO_x$ and $NiFeO_xH_y$, which gives rise to an elevated valence at the Ni sites (average oxidation state ∼ 2.37). The synthesized $NiFe/B-TiO_x$ delivers a current density of 10 mA cm^{-2} and 100 mA cm^{-2} at an overpotential of 227 mV and 268 mV, respectively, which are better than that of pure Ti and stainless steel. It also shows outstanding activity and stability under industrial conditions of 6 M KOH. The post-OER characterization studies revealed that the surface morphology and valence states have no significant change after 24 h of operation at 500 mA cm^{-2}, and also can effectively inhibit the leaching of Fe. We illustrate that surface modification of Ti which has high corrosion resistance and mechanical strength, to generate strong interactions with $NiFeO_xH_y$ is a simple and effective strategy to improve the OER activity and stability of non-precious metal electrodes.

Introduction

Electrochemical water splitting driven by renewable energy is one of the most environment friendly routes for the production of ultrapure hydrogen, also well known as green hydrogen (GH), which plays a critical role in fuel cells and energy conversions.[1,2] Currently, the main commercially available technologies for GH are alkaline water electrolysis (AWE) and polymer electrolyte membrane (PEM) electrolysis, but the former has enormous advantages in terms of scale-up because inexpensive 3d transition metal elements can be used as catalysts.[3,4] However, its energy conversion efficiency is strongly restricted by the anode reaction of the oxygen evolution reaction (OER), which is a sluggish process involving four proton-coupled electron-transfer steps.[5,6] In the last few decades, the materials used for driving the OER under alkaline conditions have made great progress; specifically, nickel–iron (oxy)hydroxides ($NiFeO_xH_y$)

were considered the most promising catalysts because of their excellent acceleration of OER dynamics and strong stability.[7–11] Moreover, it should be emphasized that the substrates for supporting $NiFeO_xH_y$ are particularly important for maintaining the stability of the whole electrode under high current density operation, as strong alkali solutions are highly corrosive liquids. For the complex process of OER, the role of the substrate is not limited to that of a current collector but it is often required to increase the adhesion strength of the catalyst to resist the shear stresses generated by the release of gas bubbles.[12] Also, a suitable substrate can induce catalyst–support interactions (CSIs) that modify the crystal and electronic structure of the catalytic sites to enhance the OER catalytic activity.[13–15]

Titanium (Ti) metal is recognized as the best substrate for electrodes due to its high corrosion resistance and mechanical strength and has been widely used and validated in dimensional stable anodes (DSAs),[16,17] which are prepared by spraying a mixture of Ru, Ir and Ti precursors onto Ti metal surfaces and subsequent pyrolysis at high temperature (commonly >400 °C).[18–20] Thanks to the high-temperature treatment, a higher electrical conductivity of $RuIrTiO_x$ solid solution is obtained by sintering Ru or Ir with Ti to form an intermediate layer, which firmly bridges the Ti substrate and the catalytic layer in DSAs.[21] However, the crystal structure of $NiFeO_xH_y$ is particularly sensitive to sintering temperature; it can be converted to a more

[a]*Key Laboratory of Agro-Forestry Environmental Processes and Ecological Regulation of Hainan Province, College of Ecology and Environment, Hainan University, 58 Renmin Road, Haikou 570228, P. R. China. E-mail: weisun@hainanu.edu.cn*

[b]*Zhejiang Provincial Key Laboratory of Water Science and Technology, Yangtze Delta Region Institute of Tsinghua University, Zhejiang, Jiaxing 314006, P. R. China. E-mail: he0207@outlook.com*

† Electronic supplementary information (ESI) available. See DOI: https://doi.org/10.1039/d3sc04858f

‡ Equal contribution.

inert oxide structure at only 300 °C,[10] so loading $NiFeO_xH_y$ on substrates is almost impossible to treat with commercial DSAs. Therefore, surface modification of the Ti substrate is necessary to enable the $NiFeO_xH_y$ catalytic layer to adhere robustly to the smooth metal Ti surface and is significant for high current density operation.

Here, we used a mild method to derive a defective blue titanium oxide ($B-TiO_x$) layer *in situ* on the surface of Ti foil and used it as a carrier for electrodeposition of $NiFeO_xH_y$ to form catalytic electrodes ($NiFe/B-TiO_x$). The $NiFeO_xH_y$ grown on the surface of $B-TiO_x$ has an amorphous structure, and in addition, advanced structural characterization studies have evidenced the existence of a significant CSI effect between them, which induces the formation of high-valent Ni and Fe, which we call a pre-oxidized state. The prepared $NiFe/B-TiO_x$ provides a compelling OER activity, which delivers a current density of 100 mA cm^{-2} in conventional 1 M and commercial grade 6 M KOH solutions with overpotentials of only 268 and 220 mV, respectively. With the help of theoretical calculations, the key active site of Ni presents a pre-oxidized state in $NiFe/B-TiO_x$ which may play a critical role in enhancing the OER activity. Moreover, $NiFe/B-TiO_x$ can be operated stably for a long time under industrial conditions of 0.5 A cm^{-2} and the post-stability characterization confirms that its morphology and compositional structures are virtually undamaged.

Results and discussion

The morphology, composition and structure of amorphous $NiFe/B-TiO_x$

Here, we use alkaline anodization to directly derive a blue titanium oxide ($B-TiO_x$) layer on the Ti foil surface, and subsequently electrodeposit $NiFeO_xH_y$ with a Ni/Fe mole ratio of 3/1 to form a Ti-based anode with a firmly adherent surface coating ($NiFe/B-TiO_x$). $B-TiO_x$ belongs to the family of colored TiO_2 and the color change originates from the oxygen defects or disorder in the lattice,[22] thereby called "self-doping".[23,24] The formation of $B-TiO_x$ often depends on a reducing atmosphere or the reducing additives in solution,[22,25] but herein it was successfully prepared by mild anodization under alkaline conditions only. We speculate that its formation may be through the following chemical process:

$$Ti^0 + OH^- \rightarrow Ti^{n+}O_x + ne + H_2O \text{ (here, } n < 4)$$
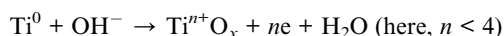
The X-ray diffraction pattern (XRD) of prepared $B-TiO_x$ is shown in Fig. 1a, in which the peaks located can be assigned to metallic Ti. Although no diffraction peaks related to Ti oxides were found in the XRD pattern, the inset photograph clearly shows that a blue covering has formed on the surface (Fig. S1†). The surface color transformation is from the formation of $B-TiO_x$.

To understand the crystal structure of $B-TiO_x$, transmission electron microscopy (TEM) was performed. As shown in Fig. S2,† it presents a sheet structure and shows clear lattice fringes, whose plane distances are very close to those of the defective

Ti_4O_7. $B-TiO_x$ derived directly on the Ti surface not only avoids the risk of poor adhesion that is associated with epitaxially grown coatings, but its defect-rich nature also contributes to the conductivity of the interface. Fig. 1b shows the scanning electron microscopy (SEM) image of $B-TiO_x$, and a rough surface can be clearly observed, which may provide a large number of attachment sites, and as a result, allow the $NiFeO_xH_y$ catalytic layer to be firmly bonded to the surface. It can be confirmed by the high-pressure tape adhesion experiments, as shown in Fig. S3,† that $NiFe/B-TiO_x$ can withstand a pressure of up to 10 MPa without shedding any catalyst on the tape, while NiFe/Ti showed almost 30% catalyst shedding from its surface at only 1 MPa. Moreover, the derivative of $B-TiO_x$ can dramatically improve the hydrophilicity of the surface, as it gives a water contact angle (WCA) of only 19.8 ± 2.4°, which is much lower than the value (97.9 ± 1.6°) of fresh Ti (Fig. S4†). The significant improvement in surface wettability may facilitate uniform electrodeposition growth of catalytic layers.

The SEM image of $NiFe/B-TiO_x$ (Fig. 1c) shows that the electrodeposition of $NiFeO_xH_y$ is well covered on $B-TiO_x$ and exhibits a morphology that is like the typical morphology of a DSA electrode.[21] The overall morphology of $NiFeO_xH_y$ catalytic films consists of larger sheet flowers and fine nanosheets, both of which are consistent with the intrinsic sheet structure of $NiFeO_xH_y$.[26,27] However, the $NiFeO_xH_y$ grown on fresh Ti shows a morphology of a woolly ball that is formed by the interlocking of numerous sheets, as clearly observed in Fig. S5.† This also suggests that the surface properties of the substrate have a huge influence on the formation of $NiFeO_xH_y$ by electrodeposition, where we speculate that it may be a result of surface wettability. It should be noted that the $NiFeO_xH_y$ catalytic films have an amorphous structure, which is evidenced by no feature peaks of $NiFeO_xH_y$ identified in either the bulk XRD or surface grazing incidence XRD patterns (Fig. 1a). The performed TEM (Fig. 1d and e) shows that the formed $NiFeO_xH_y$ exhibits a typical sheet shape, which is consistent with the observation of SEM. The atomic scale of high-resolution TEM (Fig. 1f) reconfirms that $NiFeO_xH_y$ exists in an amorphous state as no clear lattice fringes are found. Fig. S6† shows the high-angle annular dark-field scanning TEM (HAADF-STEM) image and corresponding elemental mapping images of $NiFe/B-TiO_x$, which verify the existence and homogeneous distribution of O, Ni, and Fe. The amorphous structure of $NiFeO_xH_y$ formed by electrodeposition on $B-TiO_x$ is independent of the thickness of its growth, as revealed by XRD (Fig. S7†).

Fig. 1g displays the obtained Ti 2p surface X-ray photoelectron spectra (XPS). The binding energy of Ti $2p_{3/2}$ for $B-TiO_x$ is 458.2 eV, which is shifted by about 0.2 eV towards the low binding energy relative to that of conventional TiO_2, indicating that the valence of Ti is lower than 4+, confirming that $B-TiO_x$ is an oxygen-rich defective Ti oxide. The binding energy of Ni $2p_{3/2}$ located at 855.7 eV in $NiFe/B-TiO_x$ (Fig. 1h) can be assigned to the $Ni^{2+}(OH)_2$, but it has slightly shifted towards higher energy when compared with that of NiFe/Ti. A similar phenomenon is also found in Fe $2p_{3/2}$ (Fig. 1i), the sample of $NiFe/B-TiO_x$ (712.8 eV) is shifted by about 0.3 eV relative to NiFe/Ti (712.5 eV). This suggests that a support–catalyst interaction (CSI) may be
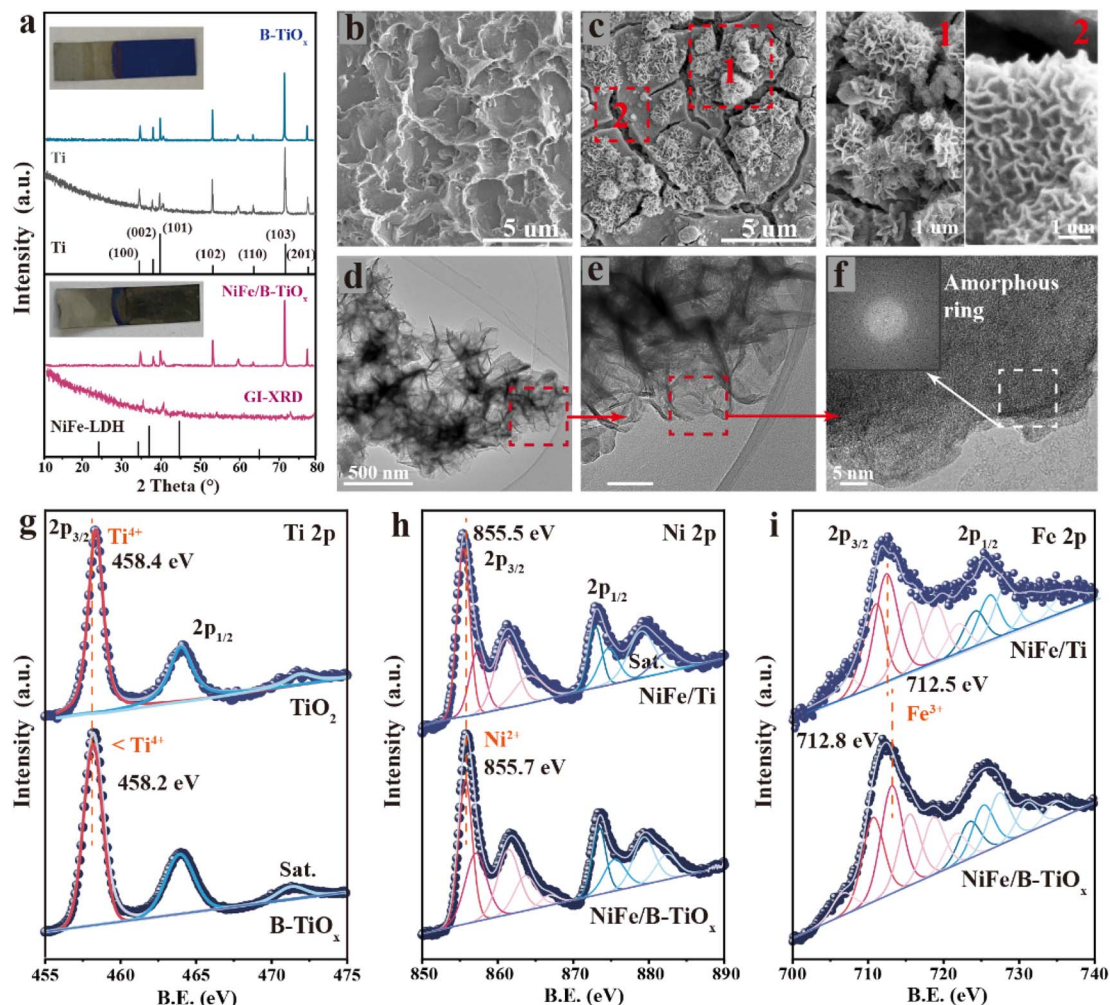
Fig. 1 (a) The XRD patterns of Ti, B-TiO$_x$ and NiFe/B-TiO$_x$. The positions of the standard diffraction peaks of Ti (pdf card number: #44-1294) and NiFe-LDH (pdf card number: #51-0463) are also marked in the figure. The insets show electronic photos of B-TiO$_x$ and NiFe/B-TiO$_x$. (b) SEM image of B-TiO$_x$. (c) SEM image of NiFe/B-TiO$_x$. The selections correspond to the microscopic morphology at high resolution. (d–f) The TEM images of NiFe/B-TiO$_x$ at different magnifications. (g) The XPS spectra of Ti 2p for TiO$_2$ and B-TiO$_x$. (h and i) The XPS spectra of Ni 2p and Fe 2p for NiFe/Ti and NiFe/B-TiO$_x$. The binding energy of the main peak for 2p$_{3/2}$ of different elements is marked in the corresponding figure.

presented, which resulted in higher valence states for Ni and Fe, caused by the B-TiO$_x$ acting as a charge acceptor. The O 1s XPS spectra (Fig. S8†) revealed a peak at 531.4 eV both in NiFe/B-TiO$_x$ and NiFe/Ti, corresponding to M–OH,[28,29] where M is the metal Ni or Fe.

Surface properties and electronic structure of NiFe/B-TiO$_x$

As observed in the element high-resolution XPS, the valence state of Ni and Fe are increased on account of the effect of CSI. Herein, XAS was performed to further investigate the oxidation states of Ni (since the test was performed on the whole electrode in fluorescence mode, the low Fe content did not allow the absorption intensity to reach the required level) over NiFe/B-TiO$_x$. It is well known that a higher oxidation state typically leads to a higher edge adsorption energy.[30–32] As shown in Fig. 2a, it can clearly be observed that the adsorption edge of Ni-K in NiFe/B-TiO$_x$ shifts to higher energy relative to that of NiFe/Ti, indicating the oxidation state of Ni > 2+ may be present in

the former. To describe the valence states of Ni in NiFe/B-TiO$_x$ as quantitatively as possible, we have plotted the valence states against the absorption edge (the absorption edge refers to the valence state obtained through Ni K-edge first derivative XANES spectra, shown in the inset of Fig. 2a) based on our data and together with previous data.[33,34] As shown in Fig. 2b, a non-linear relationship is figured out, which is in agreement with the previous findings.[33] Accordingly, the quantitative valence state of Ni in NiFe/B-TiO$_x$ and NiFe/Ti is 2.35 and 2.1, respectively. Given that the electrodeposition conditions (including the electrolyte, volume, potential, and temperature) are the same, it is expected that the high valence state of Ni in NiFe/B-TiO$_x$ may be associated with the CSI effect induced by the charger transfer between interfaces. The higher valence states of Ni can trigger the typical redox peak of Ni^{2+} to Ni^{3+} in the NiFeO$_x$H$_y$ shift towards a positive potential, which can be evidenced by cyclic voltammetry (CV) (Fig. 2c). It is well known that this redox peak is very sensitive to the amount of Fe
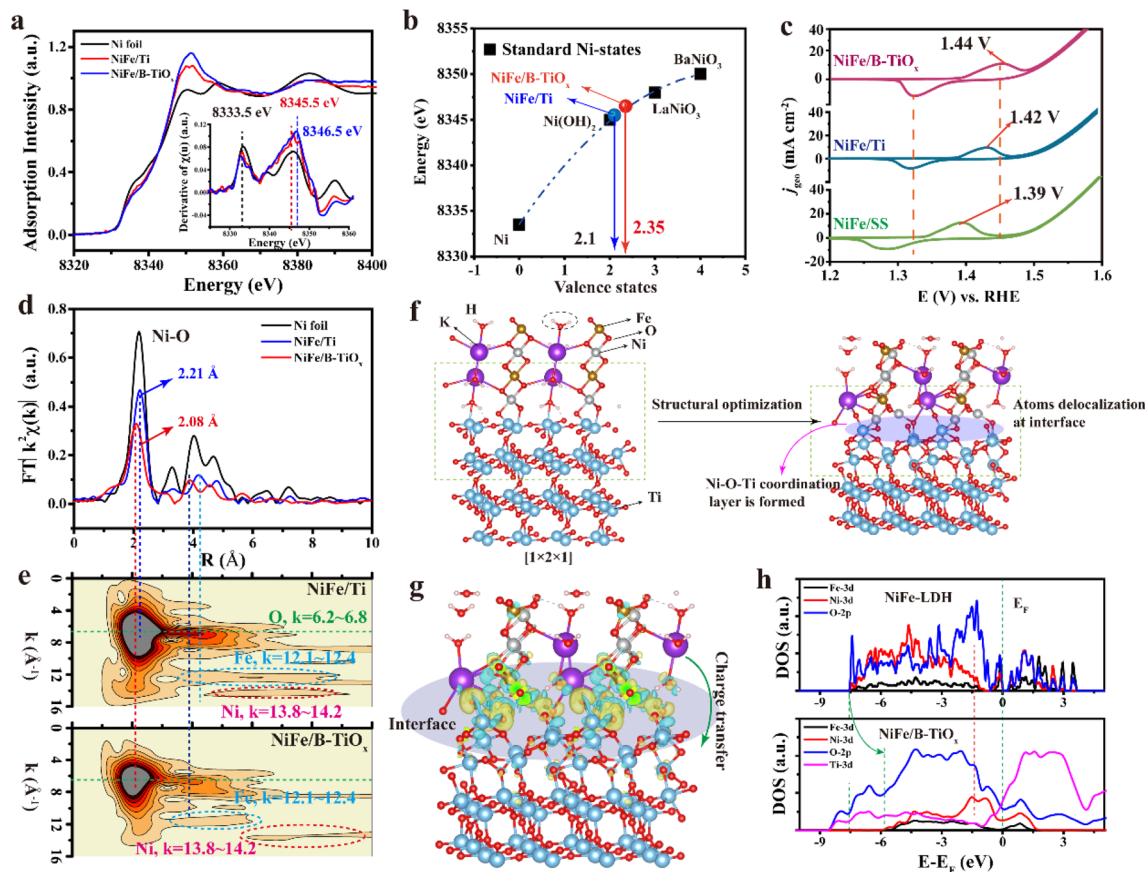
Fig. 2 (a) The normalized Ni K-edge XANES spectra. (b) Relationship between the Ni valence state and its K edge-absorption edge energy, with absorption edge energy corrected for Ni foil. (c) Cyclic voltammetry curves of three electrodes in 1 M KOH with a scan rate of 10 mV s^{-1}. The oxidation peak potential of $Ni^{2+} \rightarrow Ni^{3+}$ is labelled in the figure. (d) The k^2-FTEXAFS spectra of the Ni K-edge for different materials. The k-range of all materials is set at 2–12. (e) The corresponding k^2-weight W-MT maps of NiFe/Ti and NiFe/B-TiO$_x$. The parameters of κ and σ are 10 and 1, respectively. (f) The crystal structure of two-atomic-layer γ-NiFeOOH (100) slabs and four-atomic-layer Ti$_4$O$_7$ (102) slabs with a (2 × 1) super unit cell. (g) The differential charge analyses for a constructed model of NiFe/B-TiO$_x$. Dark yellow for charge accumulation and light blue for charge loss. (h) The DOS of NiFe-LDH and NiFe/B-TiO$_x$.

incorporated, where the peak current decreases and the peak potential increases with the increase in Fe content. The peak potentials for forward and reverse scans are located at 1.44 and 1.32 V (RHE), respectively, which are higher than that of NiFe/Ti and NiFe/SS. The *operando* XAS of potential dependence revealed that the elevated potential induces an increase in the valence state of Ni, which is the key to NiFeO$_x$H$_y$ having the catalytic OER activity.[35,36] This pre-oxidized Ni (here refers to >2+) in NiFe/B-TiO$_x$ may be more conducive to accelerated deprotonation at the OER potential and thus to enhanced activity.

The change in the average oxidation state of metal sites (here, Ni and Fe) is determined by the change in its crystal structure, such as the coordination environment, bond lengths, and defects. Here, we combine EXAFS with M-WT to investigate the crystal structure changes in Ni-sites. Fig. 2d shows the k^2-weighted backward Fourier transforms of EXAFS (k^2-FTEXAFS) spectra of the Ni-K edge. It can be clearly seen that the average bond length of the strongest NiO$_6$ coordination in NiFe/B-TiO$_x$ (2.08 Å) is lower than that of NiFe/Ti (2.21 Å). This is also verified

by the M-WT image (Fig. 2e), in which the low-value regions in k-space corresponding to the ligand O (k = 6.2–8) have lower R-values than that of NiFe/Ti. Moreover, the buzzing range of O is lower than that of NiFe/Ti, which is related to the contraction of the bond length, indirectly proving the shortening of the Ni–O bond. The shortening of the bond length represents a significant covalent bonding property,[37,38] which leads to an elevated valence state. It should be noted that no Ni–Ni or Ni–Fe coordination buzzing rings were identified in M-WT images, except for NiO$_6$, which is direct evidence that the electrodeposited NiFe-LDH has an amorphous structure, independent of the substrate chosen for deposition. It is well known that the amorphous structure can break the periodic extension of the fixed coordination,[39] and consequently, the k-space of both Fe atoms (k = 12.1–12.4) and Ni atoms (k = 13.8–14.2) in NiFe/B-TiO$_x$ and NiFe/Ti appears to be flattened and elongated, which is associated with its amorphous nature. Although both have amorphous structures, the Fe atoms of NiFe/Ti are present over a very wide R range (3–10 Å) and the Ni is between 5 and 8.4 Å; in contrast, the R spatial of Fe and Ni atoms in NiFe/B-TiO$_x$ are

staggered from each other, *e.g.*, Fe is basically concentrated in $R = 3$ to 6 Å and Ni in 6 to 10 Å, suggesting that there is also a localized ordering of the structure in NiFe/B-TiO$_x$. This deviation in atomic arrangement may be related to the nature of the substrates, but systematic studies are still needed to determine this.

To better understand the presence of charge transfer between the catalytic layer NiFeO$_x$H$_y$ and substrate B-TiO$_x$, the density functional theory (DFT) calculations are performed. The NiFeO$_x$H$_y$ phase discussed here was adopted by the widely used α-NiFe-LDH with a component of Ni : Fe = 3 : 1. It is difficult to accurately obtain the crystal structure of the direct derivative B-TiO$_x$ on the Ti surface, but previous studies revealed that the composition of the defective B-TiO$_x$ may be more consistent with that of Ti$_4$O$_7$,[22,40,41] and very close to our TEM results, so it was used here. The NiFe-LDH formed by electrodeposition tends to have a flower-like morphology formed by [003]-faceted hexagons interspersed with each other,[42] which is verified from our SEM images. Thus, the initially constructed model consists of two layers of NiFe-LDH grown radially along the [010] facets and two layers of Ti$_4$O$_7$ (Fig. 2f). After optimization, the atoms near the interface become delocalized, and a Ni–O–Ti coordination layer is formed. This variation in the interfacial structure is most likely due to a lattice mismatch in the exposed crystalline surface.[43] From Fig. 2g, there is charge accumulation around Ti and charge depletion around Ni at the interface, which evidences charge transfer between the catalytic layer NiFeO$_x$H$_y$ and substrate B-TiO$_x$, and this finding agrees with the above-mentioned XPS and XANES results.

According to the developed model for NiFe/B-TiO$_x$, its electronic structures are investigated by using the density of states (DOS), together with the pure NiFe-LDH as a comparison. As shown in Fig. 2h, the valence bands of Fe 3d and Ni 3d move towards the Fermi level (E_F) compared to that of NiFe-LDH, with an increase of about 1.5 eV. As a result, the Ni 3d bands near E_F become more localized. The resulting localization of electrons near E_F will result in a narrowed band gap between the valence and conduction bands such that the electrons from O 2p can jump into conduction bands more easily, which can contribute to modulating the binding strength of intermediates. Liu *et al.*[44] reported that narrowing the band gap of NiFe-LDH facilitates adsorption of hydroxyl ions (OH$^-$), which further improves the OER activity. Moreover, the E_F completely crosses the Ti 3d bands, which may be related to the fact that B-TiO$_x$ is endowed with more defective sites. We also found that the valence and conduction bands of Ni 3d and Fe 3d overlap with those of Ti 3d, which will help the transfer of electrons between the substrate and the catalyst, *i.e.*, the interfacial resistance may be lowered.

OER performance evaluation of NiFe/B-TiO$_x$

The OER performances of NiFe/B-TiO$_x$ were evaluated in detail under a typical three-electrode configuration with a Hg/HgO reference and a Pt foil as counter electrodes in O$_2$-saturated 1.0 M KOH, together with NiFe/Ti and NiFe/SS. The measured polarization curves (Fig. 3a) with *iR* compensation suggest that

NiFe/B-TiO$_x$ exhibits remarkable OER activity among these prepared electrodes. Apparently, it gives an overpotential as low as 220 mV to yield a current density of 10 mA cm^{-2}, considerably lower than the 258 mV and 263 mV overpotential needed for the NiFe/Ti and NiFe/SS electrodes to reach the same current density. Also, NiFe/B-TiO$_x$ just requires an overpotential of 268 mV to afford a high current density of 100 mA cm^{-2}, which is quite comparable to that of the NiFe/Ti and NiFe/SS electrodes. The OER kinetics were analysed by using Tafel plots under the electrochemical steady-state conditions (Fig. 3b), which clearly reveals that the NiFe/B-TiO$_x$ possesses a small Tafel slope of 37.5 mV dec^{-1}, much lower than that of NiFe/Ti and NiFe/SS electrodes. The compelling OER kinetics indicate that NiFe/B-TiO$_x$ has a low charge transfer resistance (R_{ct}), which can be verified by the performed electrochemical impedance spectroscopy (EIS). A low R_{ct} of 1.68 Ω was obtained in the Nyquist plots for NiFe/B-TiO$_x$, as shown in Fig. 3c and Table S1.† To confirm the high OER performance of NiFe/B-TiO$_x$, we use the electrochemical surface area (ECSA), which can be calculated by extracting the double-layer capacitance (C_{dl}) to calibrate the geometry activity to obtain the intrinsic activity of the catalytic materials, from the steady-state CV curves (Fig. S9†). Notably, NiFe/B-TiO$_x$ exhibits a high j_{ECSA} of 29.8 mA cm^{-2} at a potential of 1.53 V (Fig. 3d), which is 4 and 19 times better than that of NiFe/Ti and NiFe/SS, respectively, suggesting a huge improvement mainly originating from NiFeO$_x$H$_y$ itself.

Moreover, to better understand the highly intrinsic activity of NiFe/B-TiO$_x$, the DFT with the Hubbard-*U* approach (DFT + *U*) was employed based on the above-discussed model (four-layer NiFe-LDH and four-layer Ti$_4$O$_7$). A four-step pathway with –OH*, –O*, and –OOH* intermediates on the reaction of H$_2$O to O$_2$ was adopted to predict the OER activities of NiFe/B-TiO$_x$ and NiFe-LDH. The free energies of OER intermediates were calculated at two potentials (0 and 1.23 V), which were used to determine if the reaction trends for the free energy changes were consistent. At 0 V (Fig. 3f), the rate-determining step (RDS) of NiFe-LDH is the formation of M–O* (M–metal sites) from M–OH* with a free energy of 1.81 eV, which is consistent with the results revealed by previous DFT calculations in NiFe-LDH.[45–47] In contrast, the free energy of the second step in NiFe/B-TiO$_x$ decreases to 1.45 eV, and the RDS is M–O* to M–OOH*. The RDS of NiFe/B-TiO$_x$ and NiFe-LDH are also validated by $U = 1.23$ V, and the key energy barrier to be overcome is the third step (0.32 eV) for NiFe/B-TiO$_x$ and the second step (0.35 eV) for NiFe-LDH. The difference in the RDS indirectly demonstrates that changes in the local microcrystal structure and active site valence have a huge impact on the critical energy barriers that need to be overcome by the OER process. In predicting and designing novel catalysts for DFT applications, a linear correlation $\Delta G_{OOH*} = \Delta G_{OH*} + 3.2 \pm 0.2$ is found in various catalysts,[48–50] and this dependency is replicated in our studies (Fig. 3g). For an ideal catalyst, it is expected to be able to reconcile these competing adsorption energies without allowing the free energy of a step to be too high. The higher values of ΔG_{OH*} and ($\Delta G_{O*} - \Delta G_{OH*}$) mean too weak binding of an adsorbate over the active site,[50] as a result, impeding the adsorption of OH and increasing the energy barrier of deprotonation, which was extensively validated on
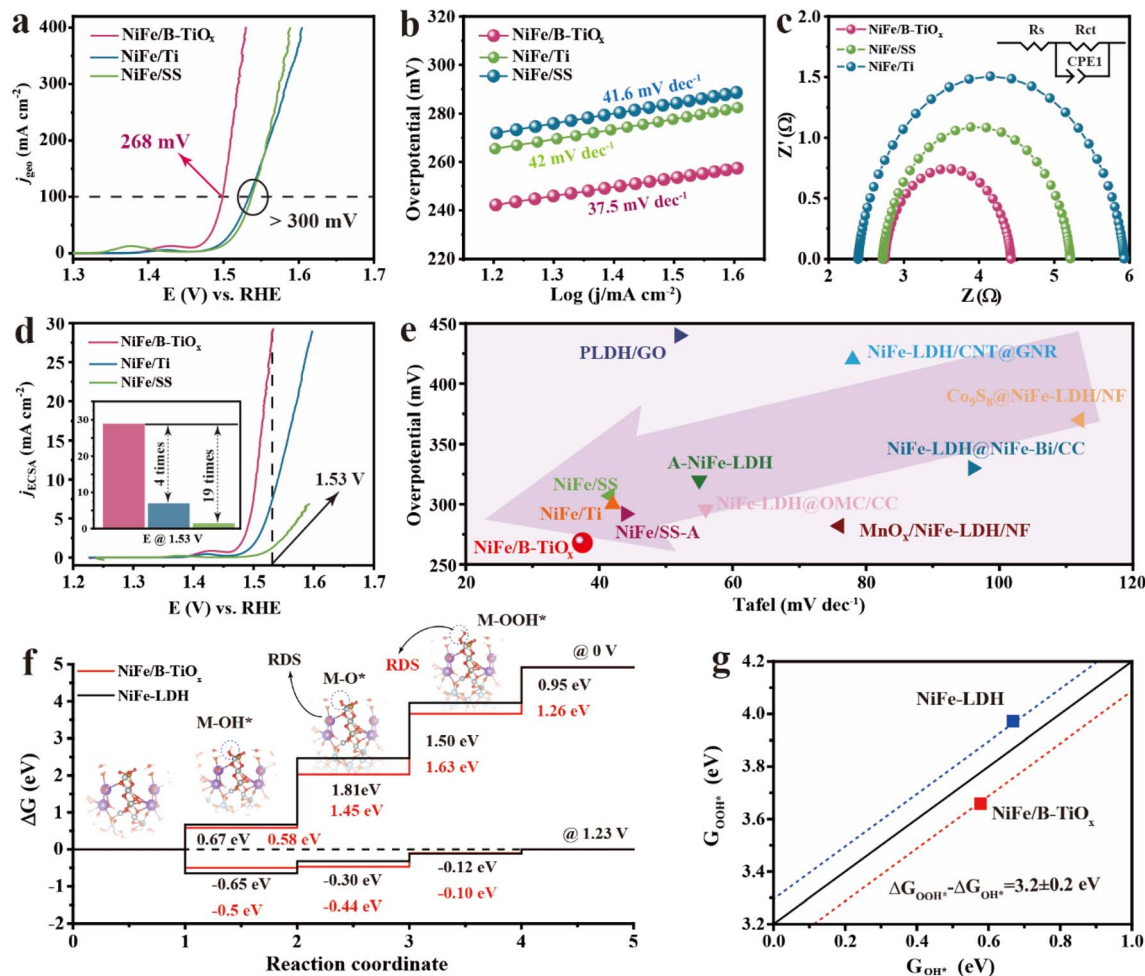
Fig. 3 (a) The OER polarization curves with *iR* compensation of NiFe/B-TiO$_x$, NiFe/Ti, and NiFe/SS. (b) The corresponding Tafel plots. (c) Nyquist plots of different electrodes at 0.6 V (*vs.* Hg/HgO). (d) ECSA-normalized polarization curves of samples to uncover the intrinsic activity of these samples. The inset shows the comparison of ECSA-normalized activity. (e) The scatter plots of the overpotential at a current density of 100 mA cm^{-2} *versus* the Tafel slope are based on the reported OER activity in various literature studies. (f) Standard free energy diagram of the OER processes on the (100) facet of NiFe-LDH and NiFe/B-TiO$_x$. The adsorption structures of the intermediates are also labeled in the figure. (g) The linear scaling relation between the free energies ΔG_{OOH*} and ΔG_{OH*} on the NiFe-LDH surfaces considered. The solid line in the center is determined by using $\Delta G_{OOH*} = \Delta G_{OH*} + 3.2$ eV.

NiFe-LDH.[51,52] For NiFe/B-TiO$_x$, it effectively mitigates the energy barrier of the deprotonation step, and the third step is only 1.61 eV, giving a low theoretical overpotential of 0.30 V ($\eta = \Delta G_{OOH*} - 1.23$ V). While constrained by the difficulty of deprotonation, NiFe-LDH gives a high theoretical overpotential of 0.58 V ($\eta = \Delta G_{O*} - 1.23$ V). This ability to accelerate deprotonation and to modulate the RDS may be related to the high valence active sites.[35] As revealed by our XAS and XPS studies, the key active site of Ni presents a pre-oxidized state in NiFe/B-TiO$_x$ which may play a critical role in enhancing the OER activity.

In addition to the pursuit of high OER activity, the long-term stability of electrodes is essential for scaling up the AWE. The stability tests were conducted by applying a constant current density of 100 mA cm^{-2} continuously for at least 100 h. The recorded potential–time curves are shown in Fig. S10,† and it can be found that no appreciable deactivation was observed for

NiFe/B-TiO$_x$ during electrolysis. Specifically, the average rate of decay of the potential over a period of 100 h is only 0.23 mV h^{-1} (the potential increases by only 23 mV in 100 h). To confirm the robust stability of NiFe/B-TiO$_x$, we also compared the change in potential before and after stability tests (Fig. S11†). At specific current densities of 10, 100, and 300 mA cm^{-2}, the potential increases after electrolysis by only 31, 23, and 17 mV, respectively. This evidence fully supports the excellent durability of NiFe/B-TiO$_x$.

OER activity and stability evaluation of NiFe/B-TiO$_x$ in 6 M KOH

The remarkable OER performances of NiFe/B-TiO$_x$ are explored in detail in a common 1 M KOH solution. However, 30% (wt%) KOH (∼6 M) is used for practical industrial applications, so we investigated the activity and stability of the prepared NiFe/B-TiO$_x$ in this solution. As shown in Fig. 4a, it delivers a current
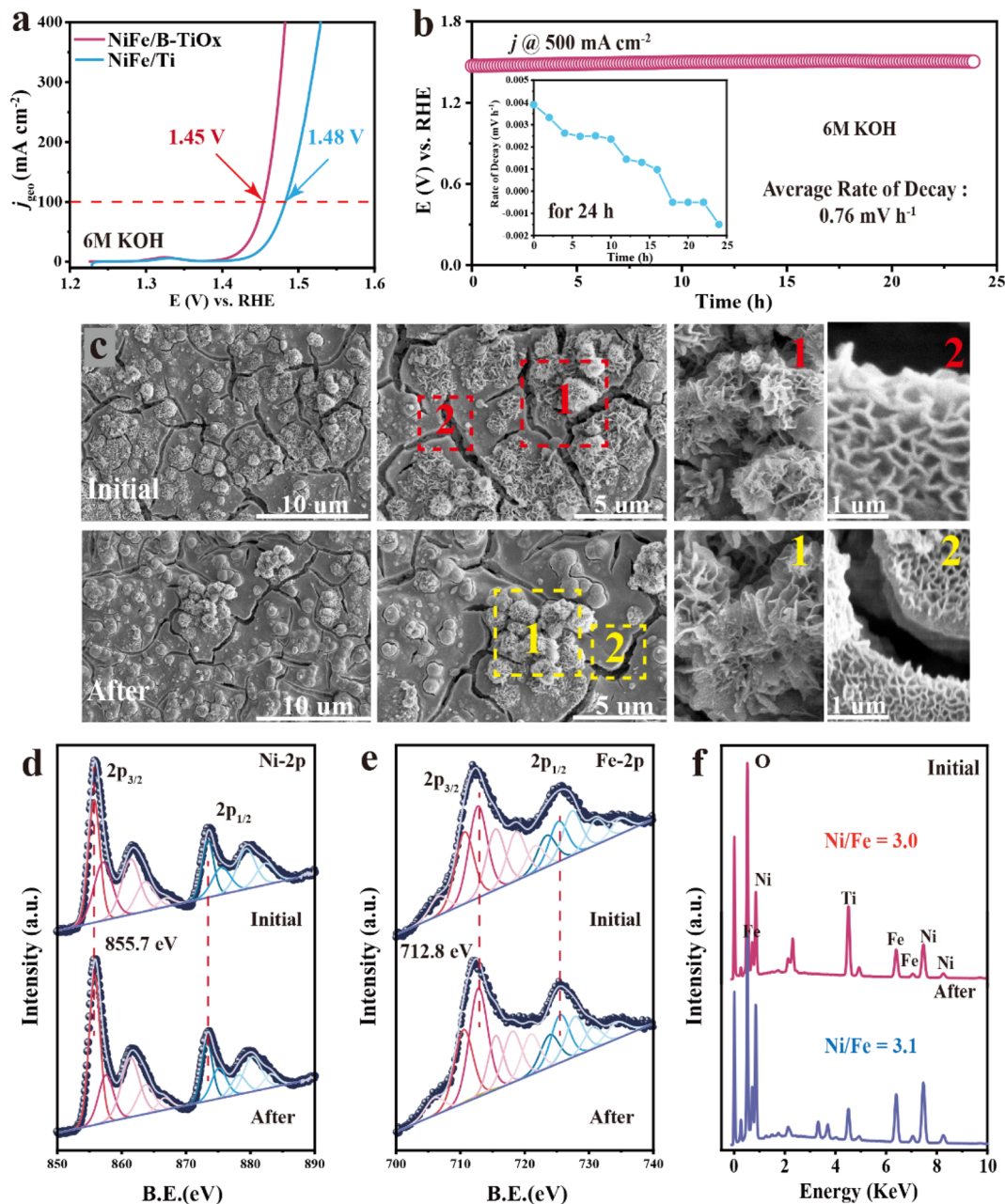
Fig. 4 (a) The OER polarizations of NiFe/Ti and NiFe/B-TiO$_x$ were determined under a 6 M KOH solution. (b) Chronopotentiometry curves of NiFe/B-TiO$_x$ at ta current density of 500 mA cm^{-2} for 24 h electrolysis. (c) SEM image comparison before and after the stability test of NiFe/B-TiO$_x$. (d and e) XPS of Ni, and Fe before and after the stability test of NiFe/B-TiO$_x$. (f) EDS characterization studies before and after the stability test of NiFe/B-TiO$_x$.

density of 100 mA cm^{-2} and 500 mA cm^{-2} at 1.45 V and 1.53 V (vs. RHE), respectively, which is 30 mV and 50 mV lower than that of NiFe/Ti. Fig. 4b shows the chronoamperometry curve for NiFe/B-TiO$_x$, which is implemented at a near industrial current density of 500 mA cm^{-2}. It can be found that there is almost no decay of the potential in up to 24 h of operation. The hour-by-hour potential decay rate decreases gradually with electrolysis time, as shown in the inset, and given a 24 h-decay rate as low as 0.76 mV h^{-1}, indicates that it possesses intrinsic stability under OER conditions. It should be pointed out that the stability of

NiFeO$_x$H$_y$ is mainly affected by the thermodynamic instability of the Fe sites[53–55] and is accompanied by a transformation of the phase structure, in particular from the active (oxy)hydroxide phase to the inert oxide phase.[56] Thereby, we carried out SEM and XPS characterization studies on the post-OER electrodes to assess possible morphological or structural changes. In terms of the morphology (Fig. 4c), no significant irreversible damage to the morphology or structure can be observed. We compared the before-and-after differences in the microscopic morphology of the edges of the cracks and the flower-like shape of the

clusters. The surface $NiFeO_xH_y$ still maintains a sheet structure consistent with the initial one. Moreover, TEM is performed to observe the morphology and structure of the $NiFeO_xH_y$. As shown in Fig. S12,† $NiFeO_xH_y$ retains a typical sheet morphology, which is consistent with that of the pristine state. In addition, $NiFeO_xH_y$ also presents an amorphous structure after the stability test, as no obvious lattice fringes are observed, indicating that $NiFeO_xH_y$ did not form the undesired inert oxide structure.

Fig. 4d and e compare the Fe- and Ni-XPS before and after 24 h electrolysis. The binding energy of the main peaks $2p_{3/2}$ and $2p_{1/2}$ for both Fe 2p and Ni 2p has no observable offset, suggesting that no phase transition occurs after the stability test. It also confirmed by the conducted O-XPS (Fig. S13†), that the surface oxygen species are still dominated by hydroxyl groups (M–OH), and no lattice oxygen was found, which implies that no inert oxides (like Fe_2O_3 or NiO) are formed. The greatest threat to the stability of $NiFeO_xH_y$ remains the irreversible dissolution of Fe, and previous studies revealed that the dissolution of Fe is not negligible even at low current density (at 10 mA cm^{-2}).[55] Here we use EDS and XPS to determine the composition change of $NiFeO_xH_y$. As shown in Fig. 4f, the bulk Ni/Fe ratio of the catalytic layer is 3.1 on the post-OER electrode, which is very close to 3.0 in the fresh one. In the most conservative scenario (i.e., EDS has a maximum error of 15%), the leaching amount of Fe is less than 8%, which is much lower than that reported in the literature.[55] Additionally, the surface compositions determined by XPS (Fig. S14 and Table S3†) show that the surface Ni/Fe molar ratio after 24 h operation at 500 mA cm^{-2} is 2.56, which is lower than that of the pristine one (2.75), which also evidences that the dissolution of Fe sites was effectively inhibited. The effective inhibition of Fe leaching over NiFe/B-TiO$_x$ may be related to the strong bonding effect between the catalytic layer and B-TiO$_x$ which substantially enhances its resistance to bubble washout. Additionally, the special atomic arrangement may also play a positive role in enhancing the intrinsic stability, because, as revealed by our W-MT, Ni and Fe atoms do not have a random arrangement but rather form with particularly localized ordering.

Conclusions

In short, mild anodization in alkaline media is a simple and effective method to form defective B-TiO$_x$ in situ on metallic Ti surfaces. Combining the results of XAS and DFT, there is a strong interaction between $NiFeO_xH_y$ and B-TiO$_x$. In particular, an interfacial charge transfer has been created, which leads to an increase of the valence state of the Ni sites. The electrochemical characterization confirms that the OER activity of NiFe/B-TiO$_x$ is greatly improved and can be operated stably for 24 h under industrial conditions of 6 M KOH, with a low potential decay rate of only 0.76 mV h^{-1}. The high valence of Ni over $NiFeO_xH_y$ turns the RDS to the third step of M–OOH from the original deprotonation step, and reconciles the free energies among the different intermediates, resulting in a lower theoretical overpotential. Post-OER characterization demonstrated that there are no significant changes in morphology and valence

structures after the stability test, and NiFe/B-TiO$_x$ exhibits the ability to inhibit the leaching of Fe. The high corrosion resistance and mechanical strength of Ti validate it to be an excellent substrate for supporting electrocatalysts, and surface modification engineering to enable strong interaction with $NiFeO_xH_y$ is a simple and effective strategy to improve the OER activity and stability of non-precious metal electrodes.

Data availability

The experimental and computational data are in the ESI.†

Author contributions

TingXi Zhou: data curation, visualization, investigation, writing – original draft, preparation. YiFei Yang: data curation. YiKe Jing: investigation. YuLing Hu: investigation. Fei Yang: supervision, software. Wei Sun: conceptualization, methodology, writing – review & editing, software, validation, supervision. LeiLei He: writing – review & editing, software.

Conflicts of interest

There are no conflicts to declare.

Acknowledgements

Notes and references

1 M. G. Walter, E. L. Warren, J. R. McKone, S. W. Boettcher, Q. Mi, E. A. Santori and N. S. Lewis, Solar water splitting cells, *Chem. Rev.*, 2010, **110**(11), 6446–6473.

2 Y. Shi and B. Zhang, Recent advances in transition metal phosphide nanomaterials: synthesis and applications in hydrogen evolution reaction, *Chem. Soc. Rev.*, 2016, **45**(6), 1529–1541.

3 S. Hu, B. Guo, S. Ding, F. Yang, J. Dang, B. Liu, J. Gu, J. Ma and M. Ouyang, A comprehensive review of alkaline water electrolysis mathematical modeling, *Appl. Energy*, 2022, **327**, 120099.

4 J. Kibsgaard and I. Chorkendorff, Considerations for the scaling-up of water splitting catalysts, *Nat. Energy*, 2019, **4**(6), 430–433.

5 N.-T. Suen, S.-F. Hung, Q. Quan, N. Zhang, Y.-J. Xu and H. M. Chen, Electrocatalysis for the oxygen evolution

reaction: recent development and future perspectives, *Chem. Soc. Rev.*, 2017, **46**(2), 337–365.

6 F. Tang, S. Guo, Y. Sun, X. Lin, J. Qiu and A. Cao, Facile synthesis of Fe-doped CoO nanotubes as high-efficient electrocatalysts for oxygen evolution reaction, *Small Struct.*, 2022, **3**(4), 2100211.

7 L. Lei, D. Huang, C. Zhou, S. Chen, X. Yan, Z. Li and W. Wang, Demystifying the active roles of NiFe-based oxides/(oxy) hydroxides for electrochemical water splitting under alkaline conditions, *Coord. Chem. Rev.*, 2020, **408**, 213177.

8 P. M. Bodhankar, P. B. Sarawade, G. Singh, A. Vinu and D. S. Dhawale, Recent advances in highly active nanostructured NiFe LDH catalyst for electrochemical water splitting, *J. Mater. Chem. A*, 2021, **9**(6), 3180–3208.

9 B. Zayat, D. Mitra, A. Irshad, A. S. Rajan and S. R. Narayanan, Inexpensive and robust iron-based electrode substrates for water electrolysis and energy storage, *Curr. Opin. Electrochem.*, 2021, **25**, 100628.

10 Z. Cai, X. Bu, P. Wang, J. C. Ho, J. Yang and X. Wang, Recent advances in layered double hydroxide electrocatalysts for the oxygen evolution reaction, *J. Mater. Chem. A*, 2019, **7**(10), 5069–5089.

11 X. Zhang, Y. Zhao, Y. Zhao, R. Shi, G. I. Waterhouse and T. Zhang, A simple synthetic strategy toward defect-rich porous monolayer NiFe-layered double hydroxide nanosheets for efficient electrocatalytic water oxidation, *Adv. Energy Mater.*, 2019, **9**(24), 1900881.

12 G. B. Darband, M. Aliofkhazraei and S. Shanmugam, Recent advances in methods and technologies for enhancing bubble detachment during electrochemical water splitting, *Renewable Sustainable Energy Rev.*, 2019, **114**, 109300.

13 Q. Liu, M. Ranocchiari and J. A. van Bokhoven, Catalyst overcoating engineering towards high-performance electrocatalysis, *Chem. Soc. Rev.*, 2022, **51**(1), 188–236.

14 M.-H. Sun, S.-Z. Huang, L.-H. Chen, Y. Li, X.-Y. Yang, Z.-Y. Yuan and B.-L. Su, Applications of hierarchically structured porous materials from energy storage and conversion, catalysis, photocatalysis, adsorption, separation, and sensing to biomedicine, *Chem. Soc. Rev.*, 2016, **45**(12), 3479–3563.

15 Q. Wang, L. Shang, R. Shi, X. Zhang, Y. Zhao, G. I. Waterhouse, L. Z. Wu, C. H. Tung and T. Zhang, NiFe layered double hydroxide nanoparticles on Co, N-codoped carbon nanoframes as efficient bifunctional catalysts for rechargeable zinc–air batteries, *Adv. Energy Mater.*, 2017, **7**(21), 1700467.

16 S. Choi, W. I. Choi, J.-S. Lee, C. H. Lee, M. Balamurugan, A. D. Schwarz, Z. S. Choi, H. Randriamahazaka and K. T. Nam, A Reflection on Sustainable Anode Materials for Electrochemical Chloride Oxidation, *Adv. Mater.*, 2023, 2300429.

17 S. Trasatti, Electrocatalysis: understanding the success of DSA®, *Electrochim. Acta*, 2000, **45**(15–16), 2377–2385.

18 G. R. P. Malpass, R. S. Neves and A. J. Motheo, A comparative study of commercial and laboratory-made Ti/Ru0.3Ti0.7O2 DSA® electrodes: "In situ" and "ex situ" surface characterisation and organic oxidation activity, *Electrochim. Acta*, 2006, **52**(3), 936–944.

19 Z. Yi, C. Kangning, W. Wei, J. Wang and S. Lee, Effect of IrO2 loading on RuO2–IrO2–TiO2 anodes: a study of microstructure and working life for the chlorine evolution reaction, *Ceram. Int.*, 2007, **33**(6), 1087–1091.

20 H. Ito and A. Manabe, Chapter 8 – Chlor–alkali electrolysis, in *Electrochemical Power Sources: Fundamentals, Systems, and Applications*, ed. T. Smolinka and J. Garche, Elsevier, 2022, pp. 281–304.

21 Z. Deng, S. Xu, C. Liu, X. Zhang, M. Li and Z. Zhao, Stability of dimensionally stable anode for chlorine evolution reaction, *Nano Res.*, 2023, 5965–5967.

22 Y. Luo and H. Lee, Present and Future of Phase-Selectively Disordered Blue TiO2 for Energy and Society Sustainability, *Nano-Micro Lett.*, 2021, **13**(1), 45.

23 J. M. Macak, B. G. Gong, M. Hueppe and P. Schmuki, Filling of TiO2 nanotubes by self-doping and electrodeposition, *Adv. Mater.*, 2007, **19**(19), 3027–3031.

24 D. Qi, L. Lu, L. Xi, L. Wang and J. Zhang, Enhanced photocatalytic performance of TiO2 based on synergistic effect of Ti3+ self-doping and slow light effect, *Appl. Catal., B*, 2014, **160**, 621–628.

25 Y. C. Nah, I. Paramasivam and P. Schmuki, Doped TiO2 and TiO2 nanotubes: synthesis and applications, *ChemPhysChem*, 2010, **11**(13), 2698–2713.

26 C. Li, Z. Zhang and R. Liu, In situ growth of 3D NiFe LDH-POM micro-flowers on nickel foam for overall water splitting, *Small*, 2020, **16**(46), 2003777.

27 S. Barwe, C. Andronescu, J. Masa and W. Schuhmann, The two Janus faces in oxygen evolution electrocatalysis: activity versus stability of layered double hydroxides, *Curr. Opin. Electrochem.*, 2017, **4**(1), 4–10.

28 C. Dong, T. Kou, H. Gao, Z. Peng and Z. Zhang, Eutectic-derived mesoporous Ni-Fe-O nanowire network catalyzing oxygen evolution and overall water splitting, *Adv. Energy Mater.*, 2018, **8**(5), 1701347.

29 C. Liang, P. Zou, A. Nairan, Y. Zhang, J. Liu, K. Liu, S. Hu, F. Kang, H. J. Fan and C. Yang, Exceptional performance of hierarchical Ni–Fe oxyhydroxide@ NiFe alloy nanowire array electrocatalysts for large current density water splitting, *Energy Environ. Sci.*, 2020, **13**(1), 86–95.

30 E. Fabbri, D. F. Abbott, M. Nachtegaal and T. J. Schmidt, Operando X-ray absorption spectroscopy: a powerful tool toward water splitting catalyst development, *Curr. Opin. Electrochem.*, 2017, **5**(1), 20–26.

31 K. Zhu, X. Zhu and W. Yang, Application of in situ techniques for the characterization of NiFe-based oxygen evolution reaction (OER) electrocatalysts, *Angew. Chem., Int. Ed.*, 2019, **58**(5), 1252–1265.

32 S. Anantharaj, S. Kundu and S. Noda, "The Fe effect": a review unveiling the critical roles of Fe in enhancing OER activity of Ni and Co based catalysts, *Nano Energy*, 2021, **80**, 105514.

33 R. J. Woolley, B. N. Illy, M. P. Ryan and S. J. Skinner, In situ determination of the nickel oxidation state in La 2 NiO 4+

δ and La 4 Ni 3 O 10− δ using X-ray absorption near-edge structure, *J. Mater. Chem.*, 2011, **21**(46), 18592–18596.

34 W. O'grady, K. Pandya, K. Swider and D. Corrigan, In situ X-ray absorption near-edge structure evidence for quadrivalent nickel in nickel battery electrodes, *J. Electrochem. Soc.*, 1996, **143**(5), 1613.

35 B. Zhang, L. Wang, Z. Cao, S. M. Kozlov, F. P. García de Arquer, C. T. Dinh, J. Li, Z. Wang, X. Zheng and L. Zhang, High-valence metals improve oxygen evolution reaction performance by modulating 3 d metal oxidation cycle energetics, *Nat. Catal.*, 2020, **3**(12), 985–992.

36 J. Kang, X. Qiu, Q. Hu, J. Zhong, X. Gao, R. Huang, C. Wan, L.-M. Liu, X. Duan and L. Guo, Valence oscillation and dynamic active sites in monolayer NiCo hydroxides for water oxidation, *Nat. Catal.*, 2021, **4**(12), 1050–1058.

37 J. Suntivich, H. A. Gasteiger, N. Yabuuchi, H. Nakanishi, J. B. Goodenough and Y. Shao-Horn, Design principles for oxygen-reduction activity on perovskite oxide catalysts for fuel cells and metal–air batteries, *Nat. Chem.*, 2011, **3**(7), 546–550.

38 F. Zhao, B. Wen, W. Niu, Z. Chen, C. Yan, A. Selloni, C. G. Tully, X. Yang and B. E. Koel, Increasing iridium oxide activity for the oxygen evolution reaction with hafnium modification, *J. Am. Chem. Soc.*, 2021, **143**(38), 15616–15623.

39 J. Gao, C.-Q. Xu, S.-F. Hung, W. Liu, W. Cai, Z. Zeng, C. Jia, H. M. Chen, H. Xiao and J. Li, Breaking Long-Range Order in Iridium Oxide by Alkali Ion for Efficient Water Oxidation, *J. Am. Chem. Soc.*, 2019, **141**(7), 3014–3023.

40 J. Wang, D. Zhi, H. Zhou, X. He and D. Zhang, Evaluating tetracycline degradation pathway and intermediate toxicity during the electrochemical oxidation over a Ti/Ti4O7 anode, *Water Res.*, 2018, **137**, 324–334.

41 T. X. H. Le, H. Haflich, A. D. Shah and B. P. Chaplin, Energy-efficient electrochemical oxidation of perfluoroalkyl substances using a Ti4O7 reactive electrochemical membrane anode, *Environ. Sci. Technol. Lett.*, 2019, **6**(8), 504–510.

42 J.-W. Zhao, Z.-X. Shi, C.-F. Li, L.-F. Gu and G.-R. Li, Boosting the electrocatalytic performance of NiFe layered double hydroxides for the oxygen evolution reaction by exposing the highly active edge plane (012), *Chem. Sci.*, 2021, **12**(2), 650–659.

43 W. Sun, Z. Zhou, W. Q. Zaman, L.-m. Cao and J. Yang, Rational Manipulation of IrO$_2$ Lattice Strain on α-MnO$_2$ Nanorods as a Highly Efficient Water-Splitting Catalyst, *ACS Appl. Mater. Interfaces*, 2017, **9**(48), 41855–41862.

44 H. Liao, G. Ni, P. Tan, Y. Liu, K. Chen, G. Wang, M. Liu and J. Pan, Borate narrowed band gap of nickel-iron layer double hydroxide to mediate rapid reconstruction kinetics for water oxidation, *Appl. Catal., B*, 2022, **317**, 121713.

45 H. Shin, H. Xiao and W. A. Goddard III, In silico discovery of new dopants for Fe-doped Ni oxyhydroxide (Ni1−x Fe x OOH)

catalysts for oxygen evolution reaction, *J. Am. Chem. Soc.*, 2018, **140**(22), 6745–6748.

46 Z. Cai, P. Wang, J. Zhang, A. Chen, J. Zhang, Y. Yan and X. Wang, Reinforced Layered Double Hydroxide Oxygen-Evolution Electrocatalysts: A Polyoxometallic Acid Wet-Etching Approach and Synergistic Mechanism, *Adv. Mater.*, 2022, **34**(26), 2110696.

47 Y. Bai, Y. Wu, X. Zhou, Y. Ye, K. Nie, J. Wang, M. Xie, Z. Zhang, Z. Liu and T. Cheng, Promoting nickel oxidation state transitions in single-layer NiFeB hydroxide nanosheets for efficient oxygen evolution, *Nat. Commun.*, 2022, **13**(1), 6094.

48 L. C. Seitz, C. F. Dickens, K. Nishio, Y. Hikita, J. Montoya, A. Doyle, C. Kirk, A. Vojvodic, H. Y. Hwang and J. K. Norskov, A highly active and stable IrOx/SrIrO3 catalyst for the oxygen evolution reaction, *Science*, 2016, **353**(6303), 1011–1014.

49 Z. Xue, X. Zhang, J. Qin and R. Liu, Revealing Ni-based layered double hydroxides as high-efficiency electrocatalysts for the oxygen evolution reaction: a DFT study, *J. Mater. Chem. A*, 2019, **7**(40), 23091–23097.

50 I. C. Man, H. Y. Su, F. Calle-Vallejo, H. A. Hansen, J. I. Martínez, N. G. Inoglu, J. Kitchin, T. F. Jaramillo, J. K. Nørskov and J. Rossmeisl, Universality in oxygen evolution electrocatalysis on oxide surfaces, *ChemCatChem*, 2011, **3**(7), 1159–1165.

51 F. Dionigi, Z. Zeng, I. Sinev, T. Merzdorf, S. Deshpande, M. B. Lopez, S. Kunze, I. Zegkinoglou, H. Sarodnik and D. Fan, In situ structure and catalytic mechanism of NiFe and CoFe layered double hydroxides during oxygen evolution, *Nat. Commun.*, 2020, **11**(1), 2522.

52 Z. W. Gao, J. Y. Liu, X. M. Chen, X. L. Zheng, J. Mao, H. Liu, T. Ma, L. Li, W. C. Wang and X. W. Du, Engineering NiO/NiFe LDH intersection to bypass scaling relationship for oxygen evolution reaction via dynamic tridimensional adsorption of intermediates, *Adv. Mater.*, 2019, **31**(11), 1804769.

53 F.-Y. Chen, Z.-Y. Wu, Z. Adler and H. Wang, Stability challenges of electrocatalytic oxygen evolution reaction: from mechanistic understanding to reactor design, *Joule*, 2021, **5**(7), 1704–1731.

54 D. Y. Chung, P. P. Lopes, P. F. B. D. Martins, H. He, T. Kawaguchi, P. Zapol, H. You, D. Tripkovic, D. Strmcnik and Y. Zhu, Dynamic stability of active sites in hydr (oxy) oxides for the oxygen evolution reaction, *Nat. Energy*, 2020, **5**(3), 222–230.

55 F. D. Speck, K. E. Dettelbach, R. S. Sherbo, D. A. Salvatore, A. Huang and C. P. Berlinguette, On the electrolytic stability of iron-nickel oxides, *Chem*, 2017, **2**(4), 590–597.

56 M. E. C. Pascuzzi, A. J. Man, A. Goryachev, J. P. Hofmann and E. J. Hensen, Investigation of the stability of NiFe-(oxy) hydroxide anodes in alkaline water electrolysis under industrially relevant conditions, *Catal. Sci. Technol.*, 2020, **10**(16), 5593–5601.